Hindawi
Advances in Civil Engineering
Volume 2023, Article ID 6650396, 17 pages
https://doi.org/10.1155/2023/6650396

Research Article

Experimental Study on the Damage and Crack Evolution Characteristics of TS-RCR Structural Bodies under Cyclic Loading and Unloading

Xiaoping Xie,[1,2] **Shanle Chen**,[1] **Xinqiu Fang**,[2] **Chengwei Liu**,[1] **Hongyang Liu**,[1] **Yuqi Huang**,[1] **Jiangang Liu**,[1,2] **and Yanfen Wang**[1]

[1]*School of Mining and Mechanical Engineering, Liupanshui Normal University, Liupanshui 553004, China*
[2]*School of Mining, China University of Mining and Technology, Xuzhou 221116, China*

Correspondence should be addressed to Shanle Chen; lb19020025@cumt.edu.cn

Received 4 January 2023; Revised 13 April 2023; Accepted 2 May 2023; Published 16 May 2023

Academic Editor: Paolo S. Valvo

Four representative TS-RCR (three-soft rock-coal-rock) structural bodies were selected according to the lithofacies analysis of coal measures in the Xiangshui Coal Mine, Guizhou, China, to analyze the mechanical properties, internal structure damage characteristics, and crack evolution law of the TS-RCR structural body composed of a soft roof, a soft floor, and soft coal seams. The mechanical model of the TS-RCR structural body was proposed. (1) The stress-strain curves of TS-RCR structures with different lithologies under cyclic loading and unloading show a change rule of sparsity, density, and sparsity with the increased cycles. The deformation of TS-RCR structures under cyclic loading and unloading can be divided into four stages. When the height ratio of the TS-RCR structural body was the same, the higher the strength of the upper and lower rocks, the more cycles the TS-RCR structural body had, and the denser the cyclic loading and unloading curve. On the contrary, the fewer cycles the TS-RCR structural body had, the sparser the cyclic loading and unloading curve. (2) The T_2 (transverse relaxation time) spectrum curves of the structural bodies were monitored at about 1 and 10 ms, and two obvious peaks were detected, indicating micropores and mesopores with a large volume in the structural body. Signal intensity increased at the relaxation time of 1 ms, decreased at 10–100 ms, and increased slightly at 100–1000 ms. The pore structure of the structural body with different lithologies changed significantly with the increased cycle number. (3) The damage and failure process of the structural body was roughly divided into three periods according to the time-history analysis of acoustic-emission AF (the ratio of acoustic-emission ringing count to duration) of the structural body: the active period with a relatively low AF value (AF < 60 kHz) in the 1^{st}-2^{nd} cycles; the rising period with a relatively stable increase of the AF value in the 3^{rd}-4^{th} cycles; and the explosive period with a relatively high AF value (AF ≥ 60 kHz) in the 5^{th} cycles. According to the relationship between the RA (the ratio of the rise time to the amplitude of the acoustic-emission-detection wave) value and time, the evolution law of the RA value and AF value of structures with different lithologies is similar in different periods under cyclic loading and unloading.

1. Introduction

The three-soft coal seam [1–4] refers to the coal seam with a soft roof, soft floor, and soft coal quality. The following requirements should be met: (1) According to [5, 6], coal seams with a sturdiness coefficient $f < 1$ are classified as weak coal seams (Platt's coefficient f, also known as the rock sturdiness coefficient and fastening coefficient, is 1/10 of the ultimate uniaxial compressive strength of rocks and is dimensionless); (2) the uniaxial compressive strength of direct roof rocks of the coal seam $\sigma \le 25$ MPa or joint spacing $d \le 60$ cm; (3) the uniaxial compressive strength of the coal seam floor $\sigma \le 25$ MPa. The roof, coal, and floor of the lower three-soft-protected coal seams form a TS-RCR structure in the pressure-relief mining process of the close-distance seam group. Influenced by engineering activities such as mining of upper protected coal seams, blasting of the adjacent chamber, roadway driving, and mining of the working face,

the TS-RCR structure bears cyclic loads [7, 8]. However, the formed TS-RCR structural body also presents different mechanical properties due to the different roof and floor lithology of the close-distance seam group. It is different from the mechanical properties of single coal and rock. The mechanical properties of the TS-RCR structural body under cyclic loading and unloading are different from those under uniaxial compression.

Ben Ammar et al. [9] studied the effects of periodic stiffness, hysteresis loop, energy dissipation, and damping on the damage density of sandwich-rich structures in different cyclic loading and unloading tests. Shkuratnik et al. [10] discussed the acoustic-emission characteristics of coal samples under different loading paths and analyzed the relationship among acoustic-emission parameters, stress, and strain. He et al. [11] and Bagde and Petroš [12] investigated the effects of cyclic loading and unloading frequencies, amplitudes, and loading rates on the fatigue mechanical properties of sandstone.

Cai et al. [13] compared the mechanical properties and acoustic-emission characteristics of coal and rock monomers, primary coal and rock masses, and synthetic coal and rock masses under uniaxial compression. Yu et al. [14] studied the uniaxial compressive strength of loose coal-rock masses. Dou et al. [15, 16] used acoustic emissions and electromagnetic radiation to monitor the uniaxial compression experiment of coal and rock masses. Besides, they analyzed the relationship between the content and strength of rocks in the coal-rock structure and the occurrence of rock bursts.

Zuo et al. [17, 18] studied the acoustic-emission characteristics of rock monomers, coal monomers, and coal-rock masses under the uniaxial compression test and the triaxial compression test. Chen et al. [19] conducted uniaxial compression tests on roof sandstone-coal pillar structures with different height ratios and studied the relationship among macrofailure initiation stress, uniaxial compressive strength, elastic modulus, and the coal-rock height ratio of roof-coal pillar structures. Wang et al. [20] used acoustic emission and microseismic to monitor the uniaxial compression test process of different coal-rock composite samples. Besides, they studied the relationship between the intensity of acoustic-emission and microseismic signals and the uniaxial compressive strength and bursting liability of the combined samples with different height ratios when impact failure occurred.

Li et al. [21] studied the influence law of coal thickness in coal-rock masses on acoustic-emission characteristics during their fracture process. Ran [22] used nuclear magnetic resonances and acoustic emissions to study the dynamic mechanical properties and damage evolution characteristics of red sandstone under cyclic impact loads. Hua [23] used an electron microscope scanner and nuclear magnetic resonance equipment to study the mechanical properties and damage evolution mechanisms of weakly consolidated sandstone under uniaxial cyclic loading and unloading.

Researchers have studied the fatigue damage of coal-rock structures under cyclic loading and unloading, their mechanical properties, and their energy evolution characteristics. However, the following problems should be solved: Research on mechanical properties and damage evolution under cyclic loading and unloading mainly focuses on a single rock or coal. There are few studies on the damage variables and cumulative damage variables of rock-coal-rock structures under cyclic loading and unloading, as well as the mechanical properties and damage evolution of TS-RCR structures with different lithologies in Guizhou Province, China, under cyclic loading and unloading. Therefore, it is necessary to study the mechanical and damage characteristics of the TS-RCR structural body with different lithologies in close-distance seam groups under cyclic loading and unloading. Uniaxial cyclic loading and unloading tests were carried out on the TS-RCR structural body of the lower protected coal seam with different lithologies to study its mechanical and damage deformation characteristics.

2. Engineering Background

The minefield of the Xiangshui Coal Mine of Guizhou Pannan Coal Development Co., Ltd. is located in Xiangshui, south of Panzhou, Guizhou, China (Figure 1). There are 13 layers of commercial coal seams from bottom to top in the minefield with a total thickness of 19.94 m and 5 layers of commercial coal seams in the whole minefield with a thickness of 12.11 m. Most commercial coal seams have 4 layers with a thickness of 3.90 m. The local commercial coal seam has 4 layers with a thickness of 3.93 m. The mine has 745.41 million tons of geological raw coal reserves, 579.51 million tons of industrial reserves, and 387.61 million tons of recoverable reserves according to the exploration. According to the outcrop profile and core data analysis of the 13^{th} layer of the commercial coal seams of the Longtan Formation in Xiangshui Coal Mine, Guizhou, China, the combination lithology of the roof and floor of the main commercial coal seam refers to weak siltstone, argillaceous siltstone, silty mudstone, and mudstone, which belong to the mining conditions of three-soft coal seams.

3. Lithofacies of the Coal Measures and Mechanical Model of the TS-RCR Structural Body

3.1. Analysis of the Lithofacies of Coal Measures. The Xiangshui Coal Mine in Guizhou Province, China, has been under construction since 2003. The mine is divided into the Hexi mining area and Botu mining area, with a designed capacity of 4 million tons/year. The exposed strata in Hexi District are coal measures of the Permian Longtan Formation, and the main exposed coal seams are $3^{\#}$, 5-$2^{\#}$, $7^{\#}$, 12-$1^{\#}$, 17-$1^{\#}$, and $19^{\#}$. The exposed strata in the soil planting area are the basalt strata of Mount Emei and the coal-measure strata of the Permian Longtan Formation. The main exposed coal seams are $3^{\#}$, 5-$2^{\#}$, 5-$3^{\#}$, $7^{\#}$, $9^{\#}$, $12^{\#}$, 17-$1^{\#}$, $19^{\#}$, $20^{\#}$, $21^{\#}$, 23-$1^{\#}$, $26^{\#}$, and $28^{\#}$. Figure 1 lists the lithofacies assemblages of the roof and floor of commercial coal seams based on the analysis of the outcrop profile and core data of the 13^{th} commercial coal seam of the Longtan Formation in the Botu mining area of the Xiangshui Coal Mine Area.

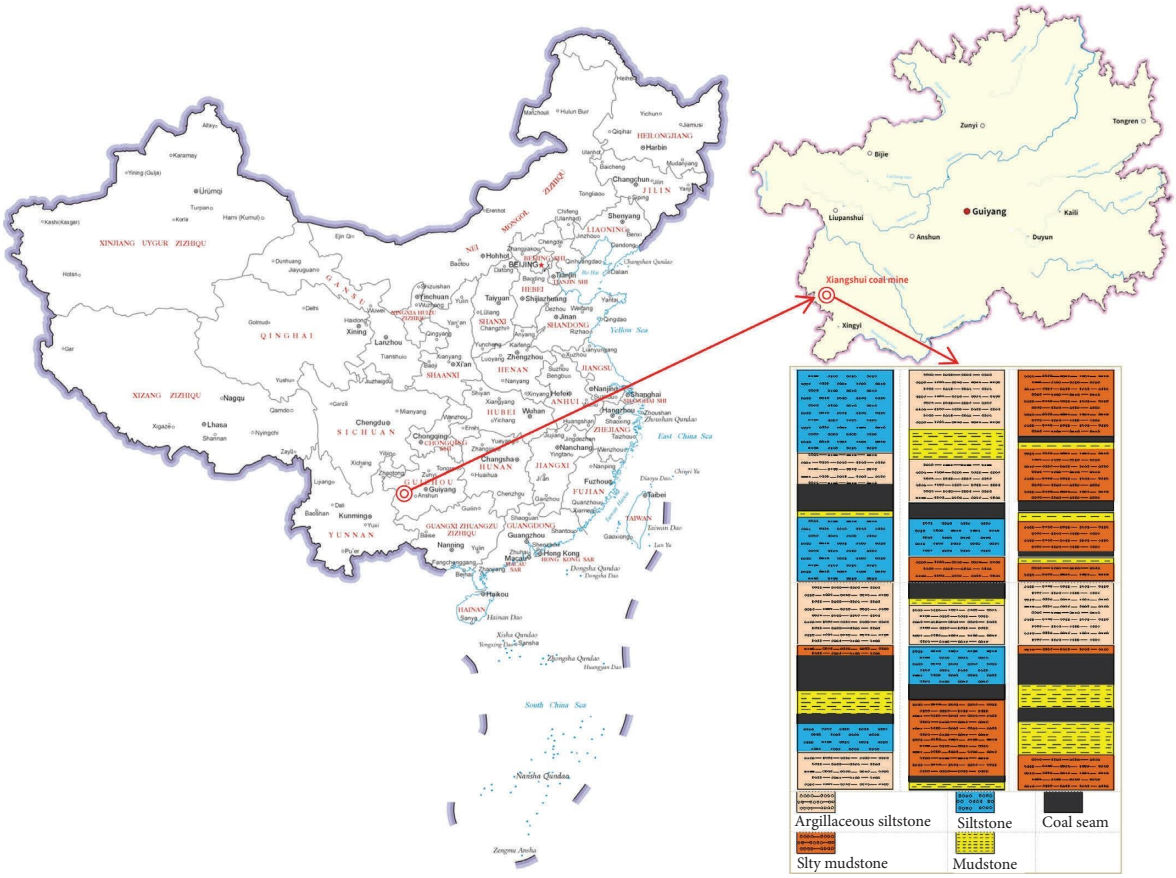

Figure 1: Combined lithology of the roof and floor of the main commercial coal seams in the Xiangshui coal mine.

The combined lithology of the roof and floor of the main commercial coal seams in Xiangshui Coal Mine is mainly composed of weak siltstone, argillaceous siltstone, silty mudstone, mudstone, and coal seam, which belong to fine deposits [24–27] in general. There are many coal layers, but most of them are of small thickness, generally less than 1.3–3.5 m. The roof and floor are dominated by thin layers of mudstone. The structure of coal seam is complex, and mudstone and carbargilite are the main sources of mining dirt. The lithofacies assemblage is relatively closer to the sea and usually develops in the tidal-flat sedimentary system. It is difficult for the combination to form thick sedimentary rocks and thick coal seams because water changes too frequently. The combination is easily affected by seawater, so thin coal seams or thinner coal seams with complex multilayer structures are developed.

3.2. Mechanical Model of the TS-RCR Structural Body. The geological conditions of Liupanshui Mine Field in Guizhou, China, are complex, with a wide distribution of high-gas coal and gas-outburst hazardous coal seams. Coal seams with the soft roof, soft floor, and soft coal are common. Common joint fractures of coal masses are developed, with low strength and loose and changeable coal masses. The immediate roof and immediate floor of the coal seam have fracture development and soft crushing. It is disturbed by engineering activities such as mining of the protected upper coal seams, blasting of the adjacent chamber, roadway driving, and mining of the working face in the mining process of the close-distance seam group. It makes the TS-RCR structural body of the lower protected coal seam subject to cyclic loading.

The TS-RCR structural body formed by it also presents different mechanical properties due to the different lithologies of the roof and floor of the close-distance seam group, which are different from the mechanical properties of single coal and rocks. The mechanical properties of the TS-RCR structural body under cyclic loading and unloading are different from those under uniaxial compression. It makes the protected coal seam rock fracture evolution, gas seepage, coal-rock pressure-relief range, and other characteristics different. Protected coal seams, roof, and floor are simplified into a TS-RCR structure. When both rocks and coal are at the linear elastic stage, the equivalent elastic modulus E of the parts of rocks and coal in series can be calculated as follows [28–33]:

$$\frac{1}{E} = \frac{1}{E_y} + \left(\frac{1}{E_m} + \frac{1}{E_y}\right)\frac{H_m}{H}, \tag{1}$$

where E, E_y, and E_m are the elastic moduli of the TS-RCR structural body, rocks, and coal, respectively. H_y and H_m are the thickness of rocks and coal, respectively, $H = H_y + H_m$.

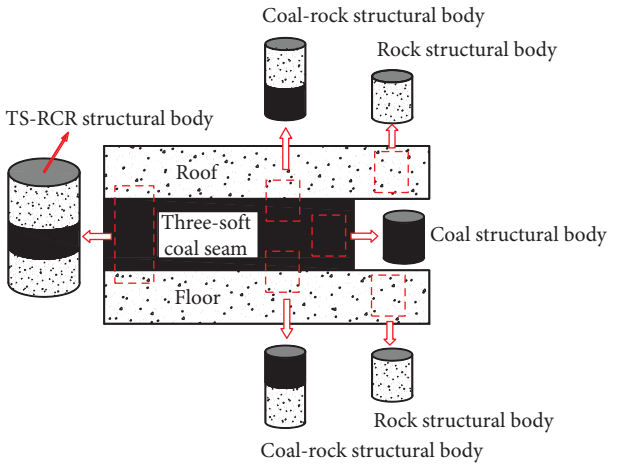

Figure 2: TS-RCR structural body model of protected coal seams.

Equation (1) is used to obtain the following equations [28–33]:

$$E = \frac{E_y}{1 + \left(E_y/E_m - 1\right)H_m/H}, \tag{2}$$

$$\sigma_j = E\varepsilon_j, \tag{3}$$

where σ_j is the stress acting on the TS-RCR structural body and ε_j is the strain generated by the TS-RCR structural body.

Equations (2) and (3) are combined to obtain the following equation [28–33]:

$$\varepsilon_j = \frac{\sigma_j}{E} = \frac{\sigma_j\left[1 + \left(E_y/E_m\right)H_m/H\right]}{E}. \tag{4}$$

When the lithology of coal and rocks constituting the TS-RCR structural body is determined, the elastic modulus E of the TS-RCR structural body is inversely proportional to the volume ratio of coal to the structural body (equation (2)). When the lithology of coal and rocks forming the TS-RCR structural body is determined, the strain ε_j produced by the TS-RCR structural body is proportional to the volume ratio of coal in the structural body under certain stress σ_j (equation (4)).

The original rock stress balance of the lower protected coal seam will be destroyed, and surrounding rock stress will be redistributed under engineering disturbances such as upper protection coal seam, adjacent roadway excavation, chamber excavation, and working face mining. Coal, roof, and floor rocks are assumed to be at the linear elastic stage. The TS-RCR structural body can be regarded as a series of roof rocks, coal, and floor rocks of the lower protected coal seam, which forms a series-combination structure. The TS-RCR structural body of the lower protected coal seam can be regarded as the model in Figure 2.

Strain produced under the same stress ($\sigma_0 = \sigma_m = \sigma_j = \sigma_y$) is ε_m, ε_j, and ε_y (Figure 3), respectively, after the stress of coal, the TS-RCR structural body, and rocks is redistributed. The equilibrium principle of elastic mechanics is used to obtain the following [28–33]:

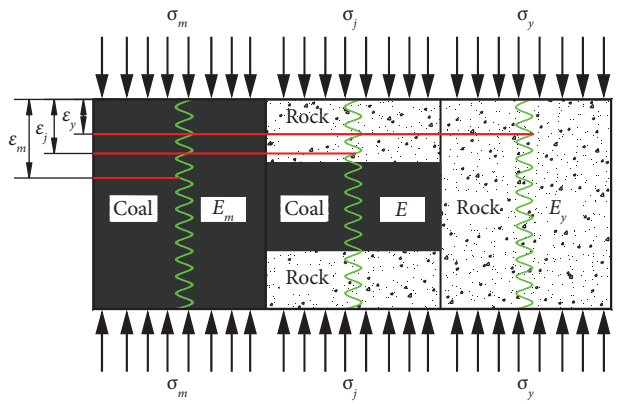

Figure 3: Mechanical model of the TS-RCR structural body.

$$\begin{aligned} \sigma_m &= \sigma = E_m\varepsilon_m, \\ \sigma_j &= \sigma = E\varepsilon_j, \\ \sigma_y &= \sigma = E_y\varepsilon_y. \end{aligned} \tag{5}$$

Strain ε_j produced on the TS-RCR structural body is compared with strain ε_m produced on the coal mass under the same stress ($\sigma_0 = \sigma_m = \sigma_j = \sigma_y$) to obtain the following equation [28–33]:

$$\frac{\varepsilon_j}{\varepsilon_m} = \frac{\sigma_j E_m}{\sigma_m E} = \frac{E_m}{E_y} + \left(1 - \frac{E_m}{E_y}\right)\frac{H_m}{H}. \tag{6}$$

Stress σ_j acting on the TS-RCR structural body is compared with stress σ_y acting on the coal mass are compared to obtain the following equation [28–33]:

$$\frac{\varepsilon_j}{\varepsilon_y} = \frac{\sigma_j E_y}{\sigma_y E} = 1 + \left(\frac{E_y}{E_m} - 1\right)\frac{H_m}{H}. \tag{7}$$

According to the coal-bearing strata of the Xiangshui coal mine in Guizhou, the elastic modulus of coal is lower than that of roof and floor rocks, that is, $E_m < E_y$.

$$1 - \frac{E_m}{E_y} > 0, \tag{8}$$

$$\frac{E_y}{E_m} - 1 > 0. \tag{9}$$

$H_m < H$ in the TS-RCR structural body. Then,

$$0 < \frac{H_m}{H} < 1. \tag{10}$$

According to equations (8) and (10),

$$\begin{aligned} \left(1 - \frac{E_m}{E_y}\right)\cdot\frac{H_m}{H} &< \left(1 - \frac{E_m}{E_y}\right) \\ 0 < \frac{E_m}{E_y} + \left(1 - \frac{E_m}{E_y}\right)\cdot\frac{H_m}{H} &< 1. \end{aligned} \tag{11}$$

According to equation (6),

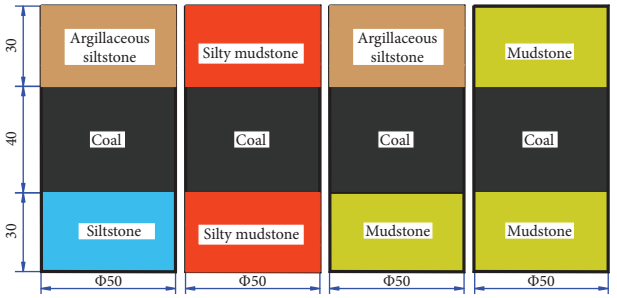

Figure 4: Design of the TS-RCR structural-body specimen (unit: mm).

$$0 < \frac{\varepsilon_j}{\varepsilon_m} = \frac{E_m}{E_y} + \left(1 - \frac{E_m}{E_y}\right) \frac{H_m}{H} < 1 \tag{12}$$

$$\varepsilon_j < \varepsilon_m.$$

According to equations (9) and (10),

$$\left(\frac{E_y}{E_m} - 1\right) \cdot \frac{H_m}{H} > 0. \tag{13}$$

Then, $1 + (E_y/E_m - 1).H_m/H > 1$.
Equation (6) is used to obtain

$$\frac{\varepsilon_j}{\varepsilon_y} = 1 + \left(\frac{E_y}{E_m} - 1\right) \frac{H_m}{H} > 1. \tag{14}$$

Then, $\varepsilon_j > \varepsilon_y$.

Based on the above analysis, strain generated under the same stress ($\sigma_0 = \sigma_m = \sigma_j = \sigma_y$) is ε_m, ε_j, and ε_y, respectively, when the stress of coal, the TS-RCR structural body, and rock is redistributed. Strain ε_y generated on rocks is less than strain ε_j generated on the TS-RCR structural body, and strain ε_j generated on the TS-RCR structural body is less than strain ε_m generated on the coal mass; that is, $\varepsilon_m > \varepsilon_j > \varepsilon_y$. The lower three-soft-protected coal seams are subjected to the same engineering disturbance stress, and the strain generated in the coal mass is maximum.

4. Cyclic Loading and Unloading Test-Specimen Production and Scheme Design

4.1. Fabrication of the Structural Body. According to the analysis of the rock facies of the coal-bearing rock system of Xiangshui Coal Mine in Guizhou, the roof and floor of the main coal mining layer are mainly weak siltstone, siltstone, siltstone, and mudstone. Therefore, four representative rock-coal-rock combination structures are selected (Figure 4). The deformations of the surrounding rocks before instability and ruptures are mainly concentrated in coal masses for mining working faces. The larger the size of the coal mass in the combined sample, the more favorable it is for observing the deformation. However, the roof and floor rocks transmit the upper and lower loads and release energy outward when the rupture occurs, so the proportion of coal masses cannot be infinitely large. Figure 4 shows the size and combination mode of the final combined sample. All coal and rock samples were taken from the same place to reduce the influence of the discreteness of coal and rock samples on the test. Coal and rock samples used in the test were taken from about 250 m of the travelling roadway of the 120519 working face of the Botu mining area of Xiangshui Coal Mine.

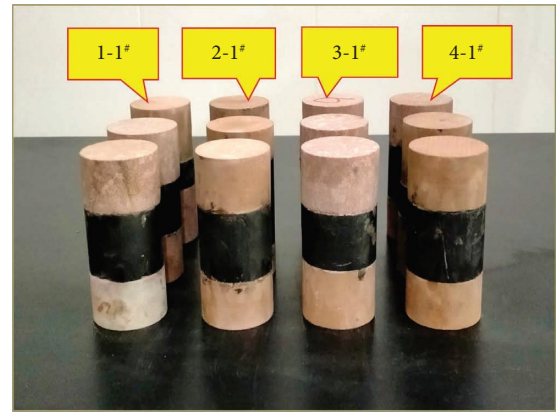

Figure 5: TS-RCR structural-body specimen.

The preparation process for the structural body specimen is as follows: Coal, siltstone, argillaceous siltstone, silty mudstone, and mudstone were drilled into a cylinder with a diameter of 50 mm with a drilling coring machine in the laboratory through on-site sampling. Then the cylinder was cut into a rock specimen with a height of 30 mm and a coal specimen with a height of 40 mm by a cutting machine. Then the combination was glued with marble glue. A grinding machine was used to grind the upper and lower end faces of the specimen into a standard one with a height ratio of 3 : 4 : 3 (with a diameter of 50 mm and a height of 100 mm). The composite structural bodies of argillaceous siltstone, coal, and siltstone were recorded as 1-1#; those of silty mudstone, coal, and silty mudstone were recorded as 2-1#; those of argillaceous siltstone, coal, and mudstone were recorded as 3-1#; and those of mudstone, coal, and mudstone were recorded as 4-1#. Each group of composite structural bodies was made of 3 specimens (Figure 5 for the sample processing).

4.2. Cyclic Loading and Unloading Test System. The cyclic loading and unloading test system mainly included the RMT-301 rock and concrete mechanics test system, the DS5 full information acoustic-emission signal analyzer, and the MicroMR12-040V nuclear magnetic resonance analyzer (Figure 6 for the test system).

4.3. Design of the Cyclic Loading and Unloading Test Scheme. According to the Chinese Coal Industry Standard MT/T174-2000 *Coal Sample Impact Tendency Classification and Index Determination Method*,' the uniaxial-compression cyclic loading and unloading test of the TS-RCR structural body specimen is carried out. The control system mainly includes displacement control and stress control. The uniaxial cyclic loading and unloading test of the TS-RCR structural body adopts the displacement control mode. The TS-RCR

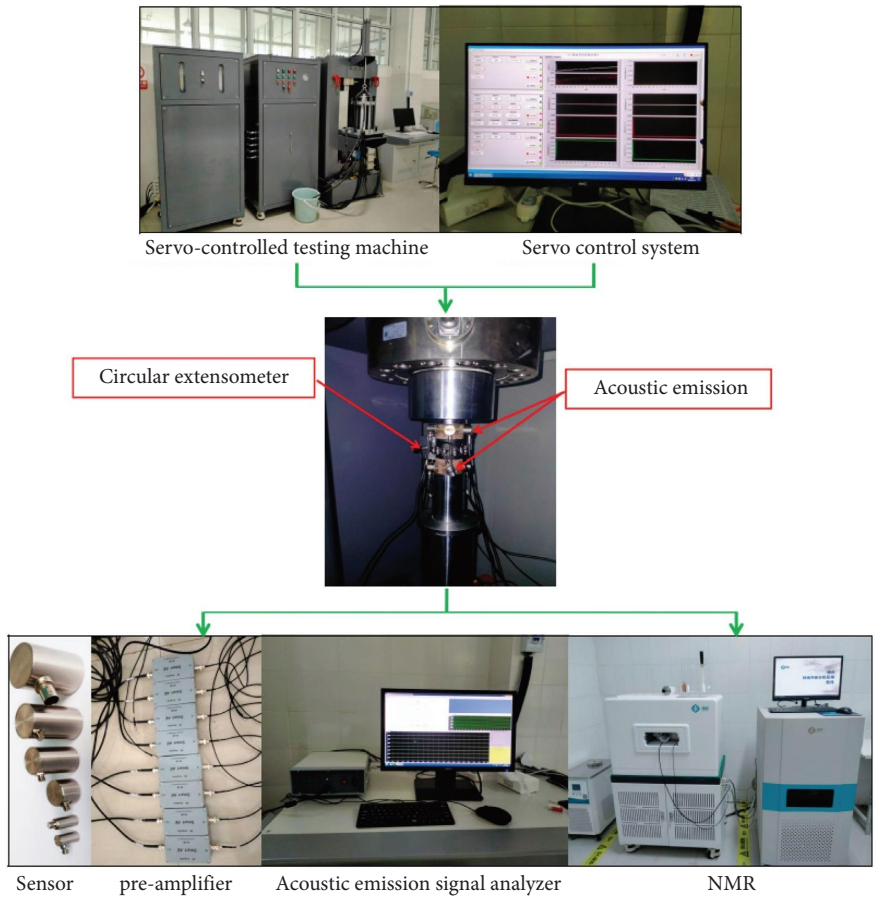

Figure 6: Compositions of the test system of the TS-RCR structural-body specimen.

structural body is placed in the middle of the test machine platform, and the initial load of the specimens is 1 kN to ensure stable contact between the specimen and the surface of the upper plate of the test machine. The displacement increment cyclic loading method with a loading rate of 0.06 mm/min is adopted. The increment of each cyclic loading is 0.1 mm and then it is unloaded to 0.01 mm. Load to 0.2 mm and unload to 0.01 mm for the next time. Repeat the above process until the structural specimen is destroyed. Figure 7 shows loading and unloading waveforms.

5. Mechanical Properties of the Composite Structural Body Specimen under Cyclic Loading and Unloading

Figure 8 shows the stress-strain curves of TS-RCR structural bodies with different lithologies during uniaxial cyclic loading and unloading tests.

The stress-strain curves of TS-RCR structures with different lithologies under cyclic loading and unloading show a change rule of sparsity, density, and sparsity with the increased cycles. The deformation of TS-RCR structures under cyclic loading and unloading can be divided into four stages: (1) The deformation rate of TS-RCR structures is small and the curve is sparse at the slow deformation stage. However, the number of cycles in this stage is small. (2) The

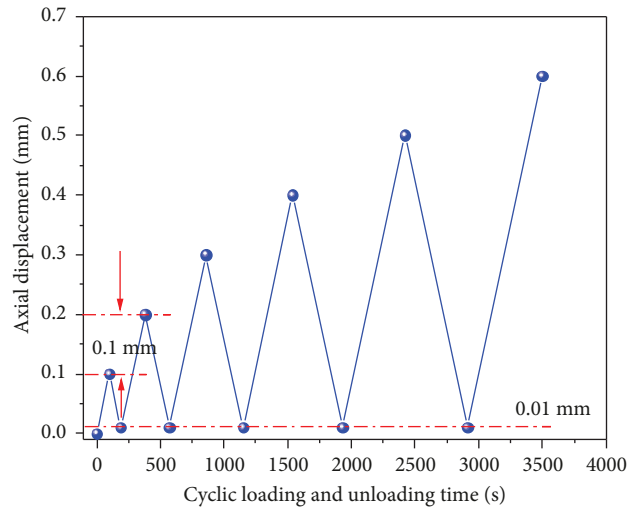

Figure 7: Uniaxial cyclic loading and unloading waveforms.

deformation and failure processes of the TS-RCR structure account for a large proportion at the uniform deformation stage. The curves in the cyclic loading and unloading processes are dense, and the deformation generated in each cycle is small and stable. (3) The strain rate of the TS-RCR structure at the accelerated deformation stage is larger than that at the first two stages. The stress-strain curves change

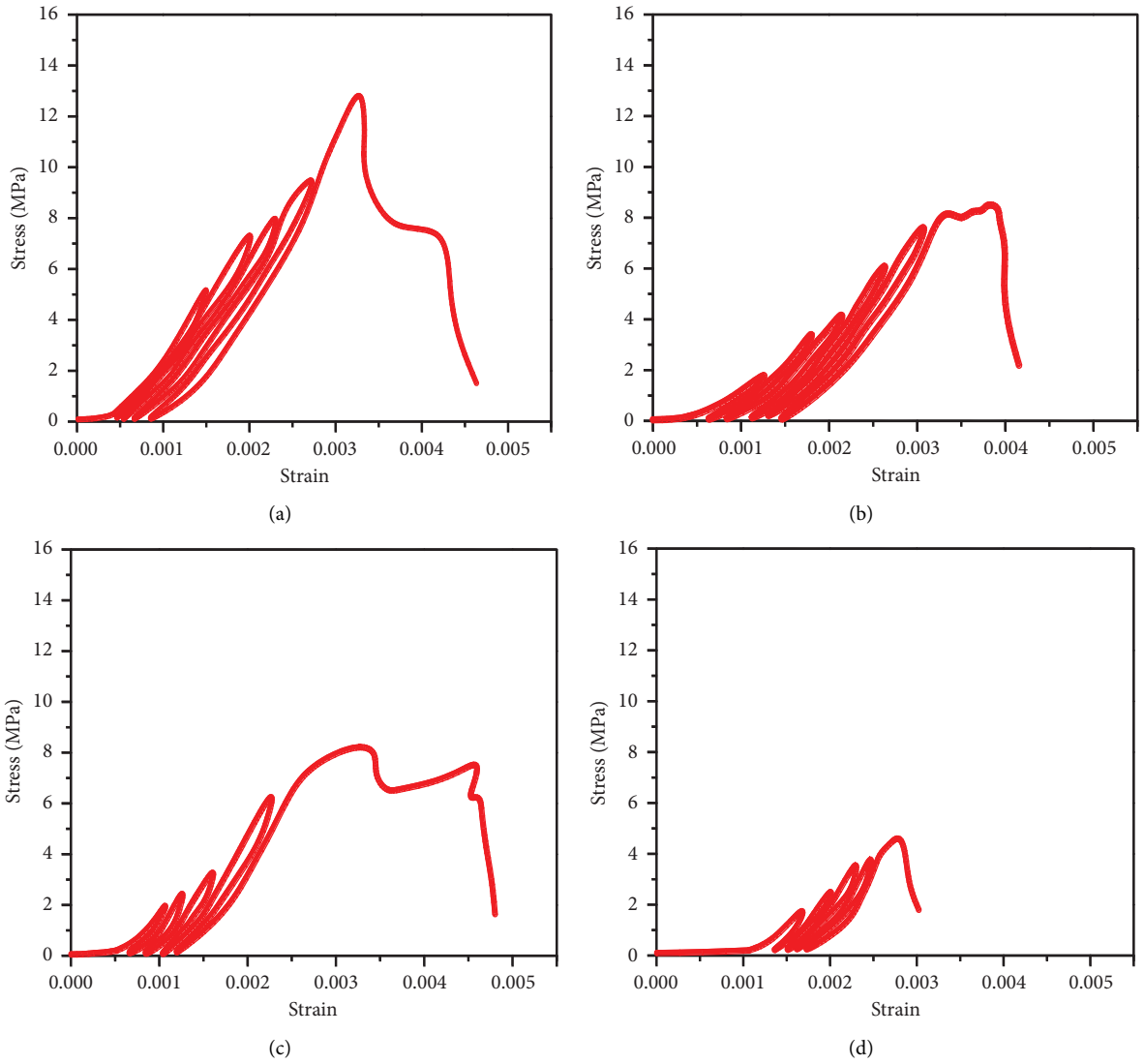

Figure 8: Stress-strain curve of the TS-RCR structural body. (a) Specimen 1-1#. (b) Specimen 2-1#. (c) Specimen 3-1#. (d) Specimen 4-1#.

from dense to sparse, with a large deformation amount generated in each cycle and few experienced cycles. (4) The TS-RCR structure after the cumulative deformation of the above three stages eventually leads to the failure of the specimens at the instability failure stage.

When the height ratios of TS-RCR structural bodies are the same, the higher the strength of the upper and lower rocks, the more the number of cycles of the TS-RCR structural body formed, and the denser the cyclic loading and unloading curve. On the contrary, the lesser the number of cycles of the TS-RCR structural body, the sparser are the cyclic loading and unloading curves. When the TS-RCR height ratio is constant, the strength of the roof, floor, and coal seam of the protected coal seam is greater, and the axial compression deformation of the structural body requires greater axial stress. It reduces the damage effect of axial stress on the whole TS-RCR structural body and increases the peak strength of the whole structural body to a certain extent. The peak strength of the TS-RCR structural body composed of siltstone and argillaceous siltstone is the largest, and the deformation caused by each cycle is small. More cycles under cyclic loading and unloading make the cyclic loading and unloading curve denser. Mudstone has low strength and large deformations. The peak strength of the TS-RCR structural body is small, and the deformation generated by each cycle is large. The number of cycles under cyclic loading and unloading is less, which makes the cyclic loading and unloading curve sparse.

6. Structural Damage and Crack Evolution Characteristics under the Cyclic Loading and Unloading

6.1. Pore Structure Evolution Characteristics Based on Nuclear Magnetic Resonance. NMR tests were conducted on the structure after 48-h forced water saturation by the MicroMR12-040V nuclear magnetic resonance analyzer to analyze the changes in the pore structure at different loading

and unloading stages of TS-RCR-structure samples under uniaxial cyclic loading and unloading.

The test operation steps are as follows: (1) Put the checked oil sample and TS-RCR structure into the magnet box successively to set the system parameters. (2) Establish marking lines with calibration samples to improve the accuracy of structural testing. (3) Put the structure into the magnet box, and use the test and analysis interface to determine the T_2 spectral curve of the structure. (4) Input measured T_2 spectral curve data, and then input the volume of the structure, that is, the porosity and pore size distribution of the structure. The structure is removed from the loading and unloading test stand after each loading and unloading. Fill with water for 1 hour, and wrap with waterproof tape to repeat the MRI test.

Pore diameters increase with increased relaxation time, and the evolution process of pore diameter distribution can be reflected by changes in the T_2 spectrum curve shapes of TS-RCR structural bodies with different lithologies [34–37]. The distribution of the porosity and pore diameters of water-saturated TS-RCR structural bodies was tested by nuclear magnetic resonance after each cyclic loading and unloading to analyze the variation of the pore structure of the TS-RCR structural body with different lithologies. Figure 9 shows the relationship between signal intensity and relaxation time T_2 of structural bodies 1-1#, 2-1#, 3-1#, and 4-1# after loading and unloading.

According to the test results, the pore size of the TS-RCR structure is divided as follows[38, 39]: small pore size ($r < 0.1\ \mu$m), medium pore size ($0.1\ \mu\text{m} < r < 1\ \mu$m), and large pore size ($r > 1\ \mu$m). The pores and cracks in the structural samples are assumed to be spherical or columnar-pipe. Then the relationship between pore radius r and relaxation time T_2 in the structure can be obtained as follows [40, 41]:

$$\frac{1}{T_2} = \rho_2\left(\frac{S}{V}\right) = \frac{\rho_2}{r}F_{\text{kx}}, \tag{15}$$

where ρ_2 is the relaxation strength of the particle surface T_2 spectrum and the ρ_2 value is related to the lithology of specimens. The value of porous medium materials is generally 1–10 μm/ms, and the value is 5 μm/ms in the work. S is the surface area of the pore, 10^{-4} m^2; V is the pore volume, 10^{-6} m^2; F_{kx} is the pore geometry factor of the specimens, 3 for spherical pores and 2 for columnar pores; and r is the pore radius of the specimens, μm.

$r = 0.1\ T_2$ is obtained by simplifying equation (15); that is, the pore radius is proportional to the T_2 value. The smaller the T_2 value, the smaller the pore.

The T_2 spectrum curves of TS-RCR structural bodies with different lithologies are monitored around 1 and 10 ms before cyclic loading and unloading, and two obvious peaks are detected (Figure 9). Peak points appear near 1 and 10 ms, and the corresponding pore radius is about 0.1 and 1 μm, indicating many micropores and mesopores in structural bodies 1-1#, 2-1#, 3-1#, and 4-1# with different lithologies. The nuclear-magnetic inversion diagram of the TS-RCR structural body changes under cyclic loading and unloading. The pore structure of the TS-RCR structural bodies with different lithologies changes significantly with the increased number of cycles. The signal intensity of the TS-RCR structural body with different lithologies at the relaxation time of 1 ms increases with the increased axial displacement of cyclic loading and unloading.

Micropores in the TS-RCR structural body are constantly developing under cyclic loading and unloading, and the peak value appears in the 2nd and 3rd cycles. The number of internal macropores is the minimum, and the TS-RCR structural body enters the continuous crack-growth stage. When the relaxation time of the TS-RCR structural body is between 10 and 100 ms, signal strength decreases. It reflects the increasing axial displacement of cyclic loading and unloading as well as the continuous compression and closure of internal pores in the TS-RCR structural body.

The signal strength of the structure increases slightly in the 4th and 5th cycles when the relaxation time is between 100 and 1,000 ms. Cracks inside the TS-RCR structural body enter the accelerated crack-propagation stage. Pore penetration intensifies, and the number of pores with large diameters increases continuously. The internal porosity of the TS-RCR structural body reaches the peak, and the damage degree reaches the maximum, indicating that the TS-RCR structural body is about to be destroyed.

6.2. Porosity Variation Characteristics of the TS-RCR Structural Body Based on Nuclear Magnetic Resonance. Uniaxial cyclic loading and unloading tests were carried out on structural bodies 1-1#, 2-1#, 3-1#, and 4-1# with different lithologies, and then nuclear magnetic resonance tests were carried out. Figure 10 shows the NMR scanning images of the TS-RCR structural bodies with different lithologies, and Figure 11 presents the variation curves of the porosity of TS-RCR structural bodies after inversion with the number of cycles.

Pores exist among the grains of TS-RCR structural body specimens with different lithologies, and the grain boundaries are clear (Figure 10). The internal pores of the TS-RCR structural body increase with the increased axial displacement of loading and unloading. As the strength of the upper and lower rock masses decreases, pore development and expansion are more likely to occur under the same coaxial displacement. Pores inside structural body 1-1# mainly occur in the central coal body, while the upper argillaceous siltstone and lower siltstone have fewer pores (Figure 10(a)). Pores inside the structural bodies 2-1#, 3-1#, and 4-1# mainly occur in the central coal body, and the upper and lower rock bodies also have pores (Figures 10(b)–10(d)). The pore scope increases with the weakened strength of upper and lower rock bodies.

The pore diameter distribution of structural bodies 1-1#, 2-1#, 3-1#, and 4-1# with different lithologies is dominated by micropores (0–0.1 μm), which account for 7.23–8.46%, 6.22–8.12%, 7.87–8.94%, and 6.19–8.11% of the total volume, respectively (Figure 11). As the TS-RCR structural body is subjected to cyclic loading and unloading, changes in micropores, mesopores, and macropores of the TS-RCR structural body with different lithologies are as follows:

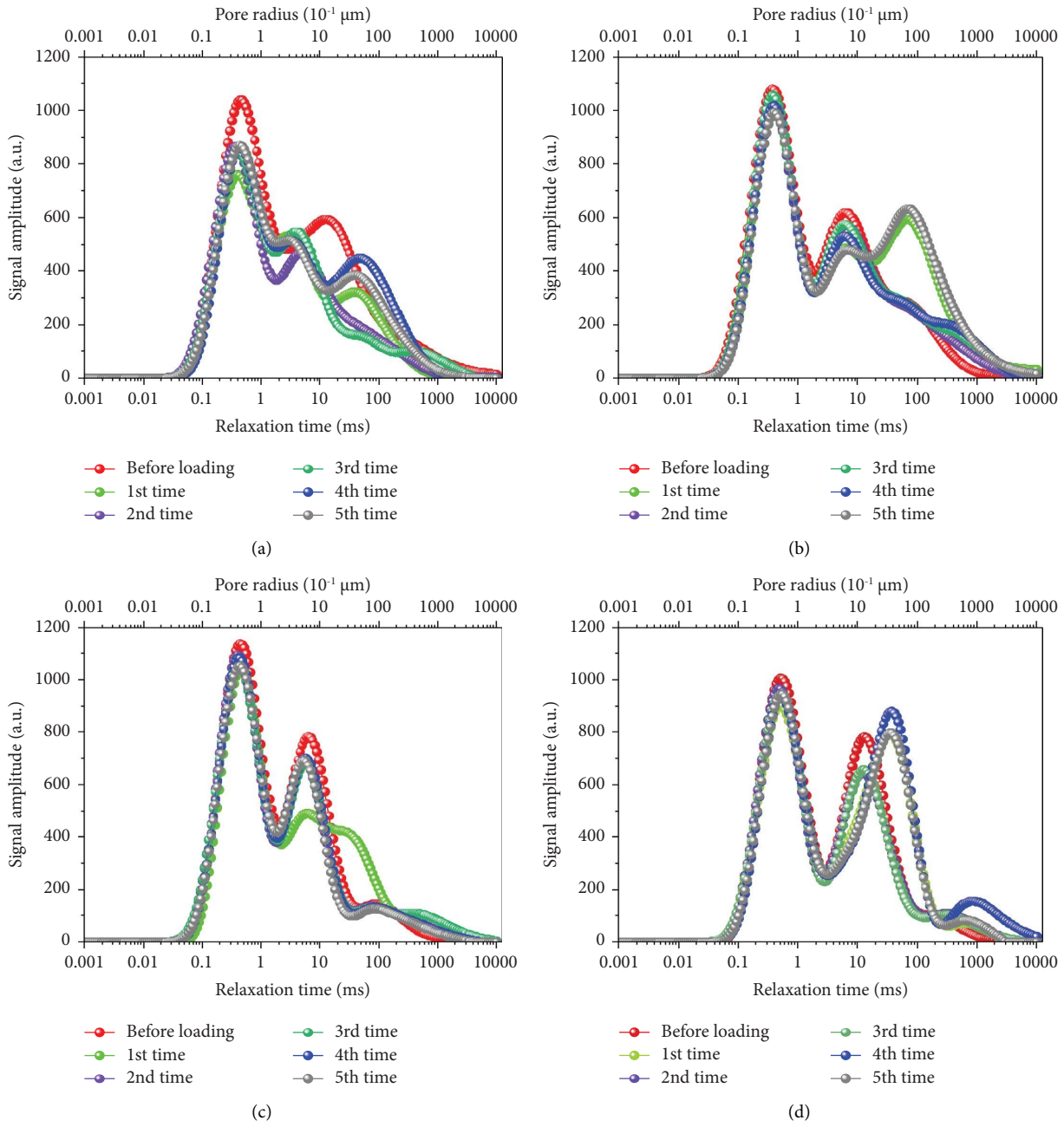

Figure 9: Relationship curve between the signal amplitudes and relaxation time of the TS-RCR structural body with different lithologies. (a) Specimen 1-1#. (b) Specimen 2-1#. (c) Specimen 3-1#. (d) Specimen 4-1#.

(1) Micropores inside the TS-RCR structural body generally show fluctuations of decreasing, rising, decreasing, and rising. As the lithology strength of the TS-RCR structural body gradually decreases, fluctuations become more obvious. The fluctuation of structural body 1-1# is weak, and the fluctuations of structural bodies 2-1#, 3-1#, and 4-1# are strong. As the lithologic strength of the TS-RCR structural body gradually decreases, micropores are more easily transformed into mesopores under cyclic loading and unloading, which decreases micropores. New micropores are generated with the further increased load, which increases micropores. It repeats until the structure is destroyed.

(2) Mesopores (0.1–1 μm) inside the TS-RCR structural body generally show fluctuations of rising, decreasing, rising, and decreasing. This characteristic is opposite to the fluctuation of micropores. The micropores of the structural TS-RCR body gradually change into mesopores under cyclic loading and unloading, which increases mesopores. As the load further increases, mesopores change into macropores. It repeats until the structure is destroyed.

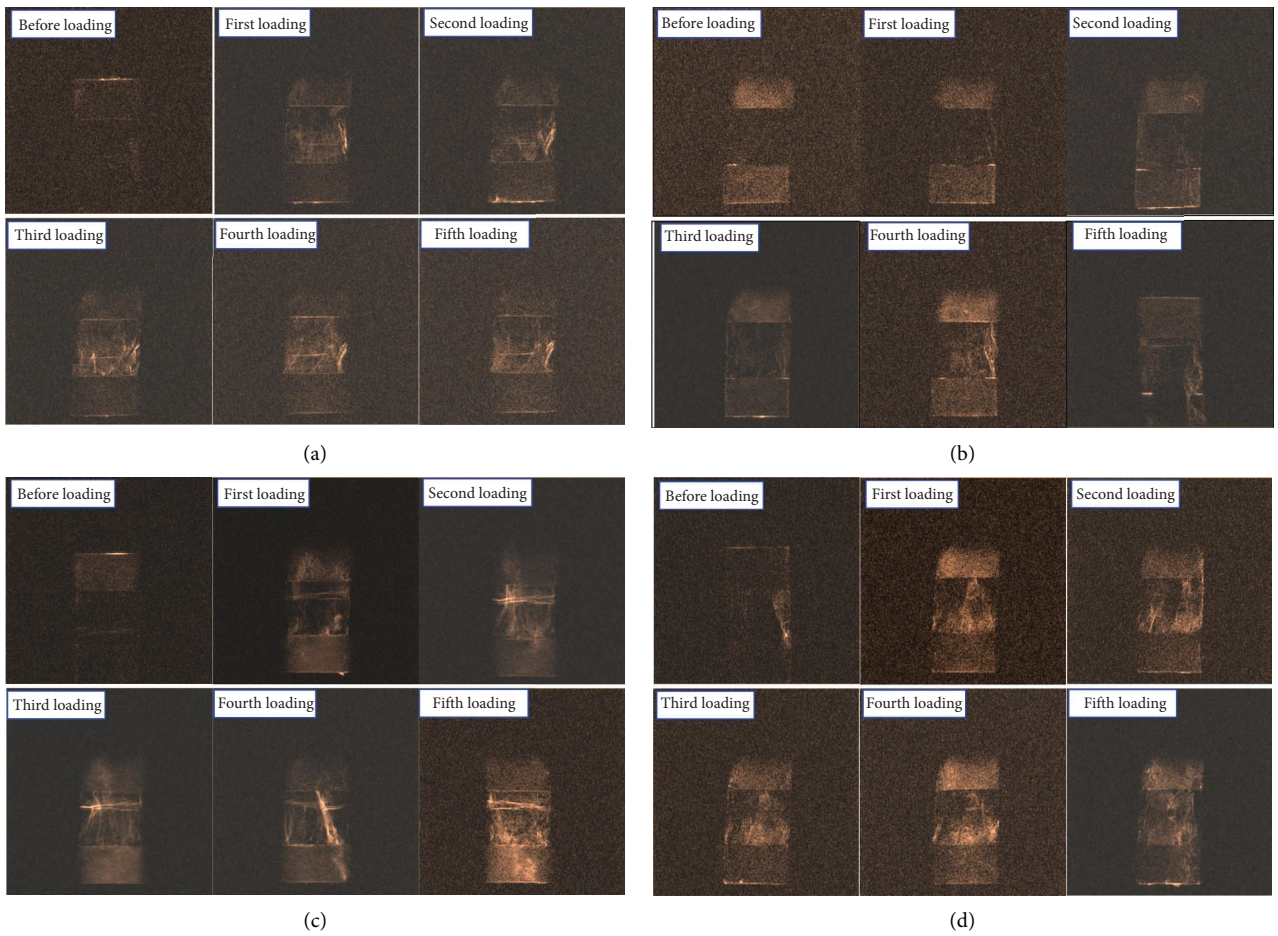

Figure 10: Scanning of the TS-RCR structural body with different lithologies before and after cyclic loading and unloading. (a) Specimen 1-1#. (b) Specimen 2-1#. (c) Specimen 3-1#. (d) Specimen 4-1#.

(3) The proportion of macropores (1–25 μm) in the structure first decreases and then increases. The final increment values of macropores in structural bodies 1-1#, 2-1#, 3-1#, and 4-1# with different lithologies are 0.02, 0.11, 0.09, and 0.74%, respectively. The final macropores of the TS-RCR structural body increase gradually with decreased lithological strength. Mesopores inside the TS-RCR structural body are compressed and destroyed with the increased load, and a short downward trend occurs. As the load continues to increase, mesopores are destroyed and combined to form macropores. Besides, it is more prone to damage and failure with the decreased lithologic strength of the TS-RCR structural body, which results in the expansion and penetration of internal cracks and increased porosity.

6.3. Crack Evolution Characteristics of the TS-RCR Structural Body Based on Acoustic Emissions. The DS5-8b acoustic emission detector was used to collect the waveform variation characteristics of the structure during the test and to analyze the growth of different microcracks in the structure under cyclic loading and unloading. Acoustic emission sensors were symmetrically arranged at the upper and lower ends of samples, with blue dots 1-8# in Figure 12.

A coupling agent was used for coupling to prevent acoustic-emission signals from losing signals due to poor contact, and elastic tapes were used for fixing to prevent dropping in the test process. The waveform characteristics of the cracking process were also collected for mechanical signals and acoustic-emission data during the test. The acoustic-emission sampling frequency was 3 MHz, with a threshold value of 50 dB and a preamplifier of 40 dB.

According to the experimental study of Wu et al. [42–44], initial microcracks inside the structure are under shear stress, and their tip expands. The AF value of the detected wave signal collected by acoustic emissions was low, and vice versa. The AF value [45–50] is defined as the ratio of acoustic-emission ringing count to duration, and its unit is KHz. Figure 13 shows the time history of acoustic-emission AF values of the TS-RCR structural bodies with different lithologies.

According to Chong et al. [51–56], the acoustic-emission detection wave properties of concrete specimens under four-point bending conditions are studied based on the resonant sensor. The acoustic-emission-

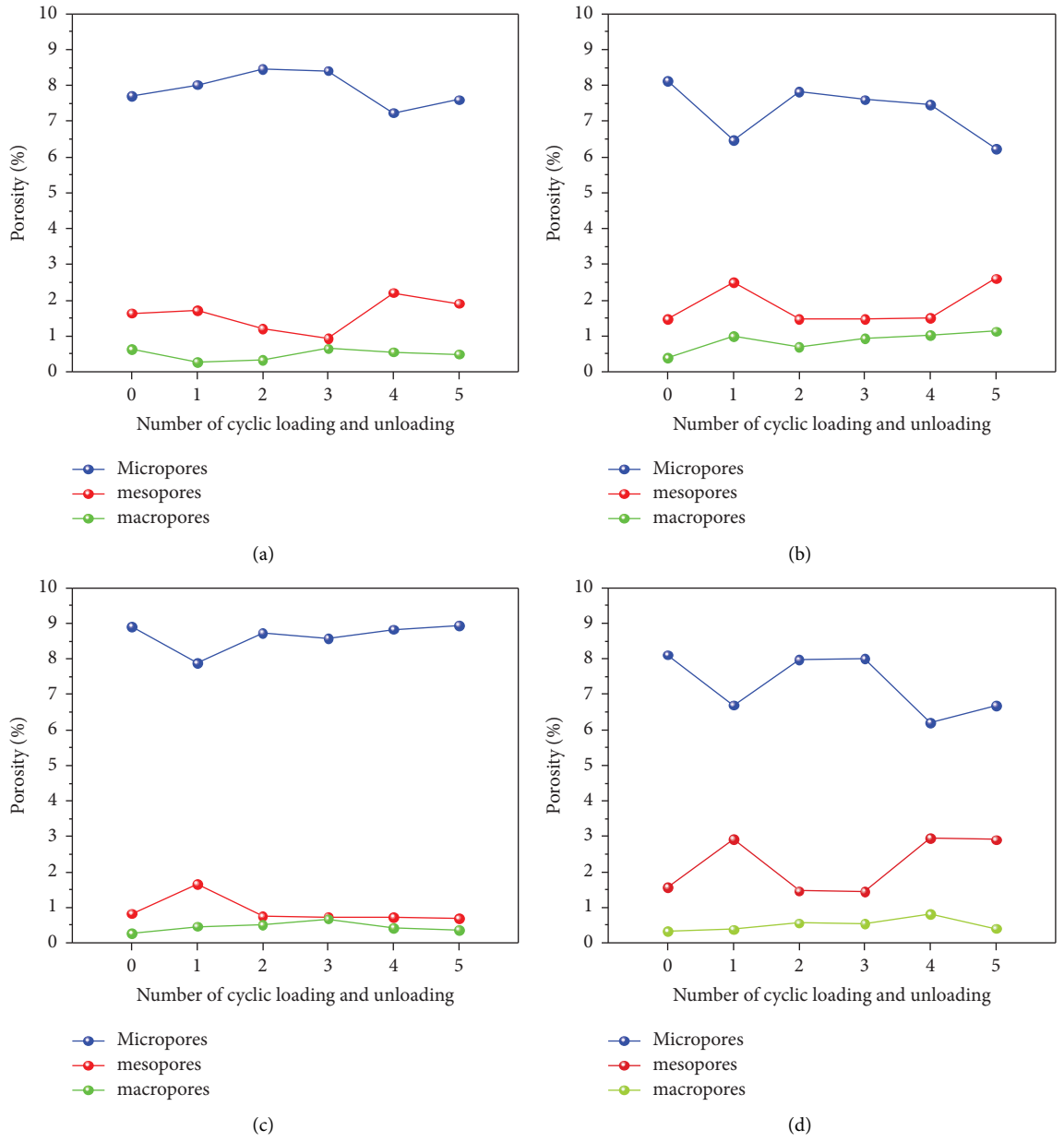

Figure 11: Porosity curve of the TS-RCR structural body with different lithologies changing with cycle times. (a) Specimen 1-1#. (b) Specimen 2-1#. (c) Specimen 3-1#. (d) Specimen 4-1#.

detection wave signals of tension and shear cracks are defined as follows [57, 58]: The range of tension cracks is $RA < 2\,ms{\cdot}v^{-1}$, and $AF > 60\,kHz$; that of shear cracks is $RA \geq 2\,ms{\cdot}v^{-1}$, and $AF \leq 60\,kHz$.

According to Figure 13, the damage and failure process of the structural body is roughly divided into three periods according to the time-history analysis of the acoustic-emission AF (the average frequency of a wave signal) value of the structural body: the active period with the relatively low AF value ($AF < 60\,kHz$) in the 1st and 2nd cycles, the rising period with the relatively stable increased AF value in the 3rd and 4th cycles, and the explosive period with the relatively high AF value ($AF \geq 60\,kHz$) in the 5th cycle.

(1) The crack evolution law in the active period of the AF value is as follows: The AF values of structural bodies 1-1#, 2-1#, 3-1#, and 4-1# with different lithologies increase with the increased axial displacement of loading and unloading. The gradual expansion, intersection, and compaction of pores, microcracks, and defects occur inside the structural body, with a small number of new cracks. The damage cracks of structural bodies 1-1#, 2-1#, 3-1#, and 4-1# are mainly tensile, and a few shear cracks occur in the inner part of structural body 4-1#.

(2) The crack evolution law at the ascending period of the AF value is as follows: As the axial displacement of loading and unloading increases, the

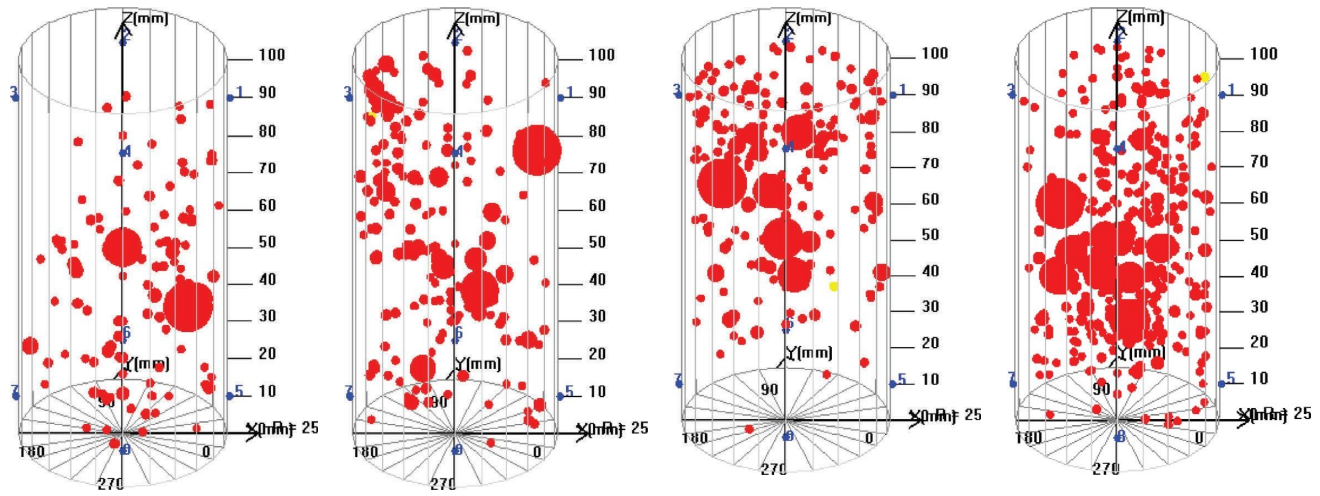

FIGURE 12: Acoustic emission damage location of the TS-RCR structural body with different lithologies. (a) Specimen 1-1#. (b) Specimen 2-1#. (c) Specimen 3-1#. (d) Specimen 4-1#.

accumulation of old cracks and the propagation of new cracks occur in the TS-RCR structural body with different lithologies. The microcracks and the structure of the TS-RCR structural body are readjusted, and stress is redistributed. The damage to cementation and crystalline granular minerals inside the TS-RCR structural body is mainly caused by tension cracks. The evolution law of AF values of the TS-RCR structural body with different lithologies is roughly the same.

(3) The crack evolution law of AF values during the burst period is as follows: A large number of AF values less than 60 kHz are gathered with the further increased axial displacement of loading and unloading. AF values increase sharply, which results in the occurrence of an AF value (>60 kHz) aggregation area before the macroscopic failure of the TS-RCR structural body. The number of new microcracks in the TS-RCR structural body increases under cyclic loading and unloading with weakened lithology in the upper and lower parts of the TS-RCR structural body, and the internal microcracks and the structure will be readjusted. Time is prolonged, and energy accumulation increases in the process of stress redistribution. It generates more new shear cracks and finally makes the structure present tensile and oblique shear failure on the macroscopic fracture.

The RA value [57, 58] is defined as the ratio of the rise time to the amplitude of the acoustic-emission-detection wave, ms/V. Figure 14 shows the acoustic-emission RA time histories of structures with different lithologies.

According to the time-history diagram analysis of the acoustic-emission RA values of structures with different lithologies in Figure 14, the acoustic-emission RA values of 1-1#, 2-1#, 3-1#, and 4-1# structures with different lithologies are less than 2 ms·v^{-1}. Only the 4-1# structure has RA values slightly greater than 2 ms·v^{-1} during the 4th-5th cyclic loading and unloading. Therefore, the structural damage and failure process can be roughly divided into three periods. The period of the relatively high RA value in the first 1-2 cycles is divided into the active period; the period of the relatively stable rise of the RA value in the middle 3-4 weeks is divided into the rising period; and the period of the peak RA value in the last fifth cycle is divided into the transition period.

According to the relationship between the RA value and time, the evolution law of the RA value and AF value of structures with different lithologies in different periods under cyclic loading and unloading is similar. The damage and failure processes of structures can be roughly divided into the active period, ascending period, and transition period. There is a slight difference between the RA value interval and the RA value due to the changes in the discriminant way of dividing the AF value interval. Specifically, the transition period of the RA value is changed to the burst period of the AF value.

According to the RA value, the value of damage failure tensile and shear cracks in the structure during cyclic loading and unloading is much lower than that of the AF value. The main reason is that the way to define and delimit the range of the AF value is different from that of the RA value. The AF value and RA value are significantly different under multiple factors, such as ringing count-duration time and rising time amplitude. Combined with the comparative analysis of the macroscopic fracture characteristics of structures, the evolution law of the RA and AF values is consistent with the macroscopic fracture characteristics of structures.

6.4. Damage Location Analysis of the Structural Body Based on Acoustic Emission. The acoustic-emission test was used to analyze the internal damage location of the TS-RCR structural bodies of different lithologic structures after cyclic loading and unloading to analyze the internal damage characteristics of the TS-RCR structural body with different

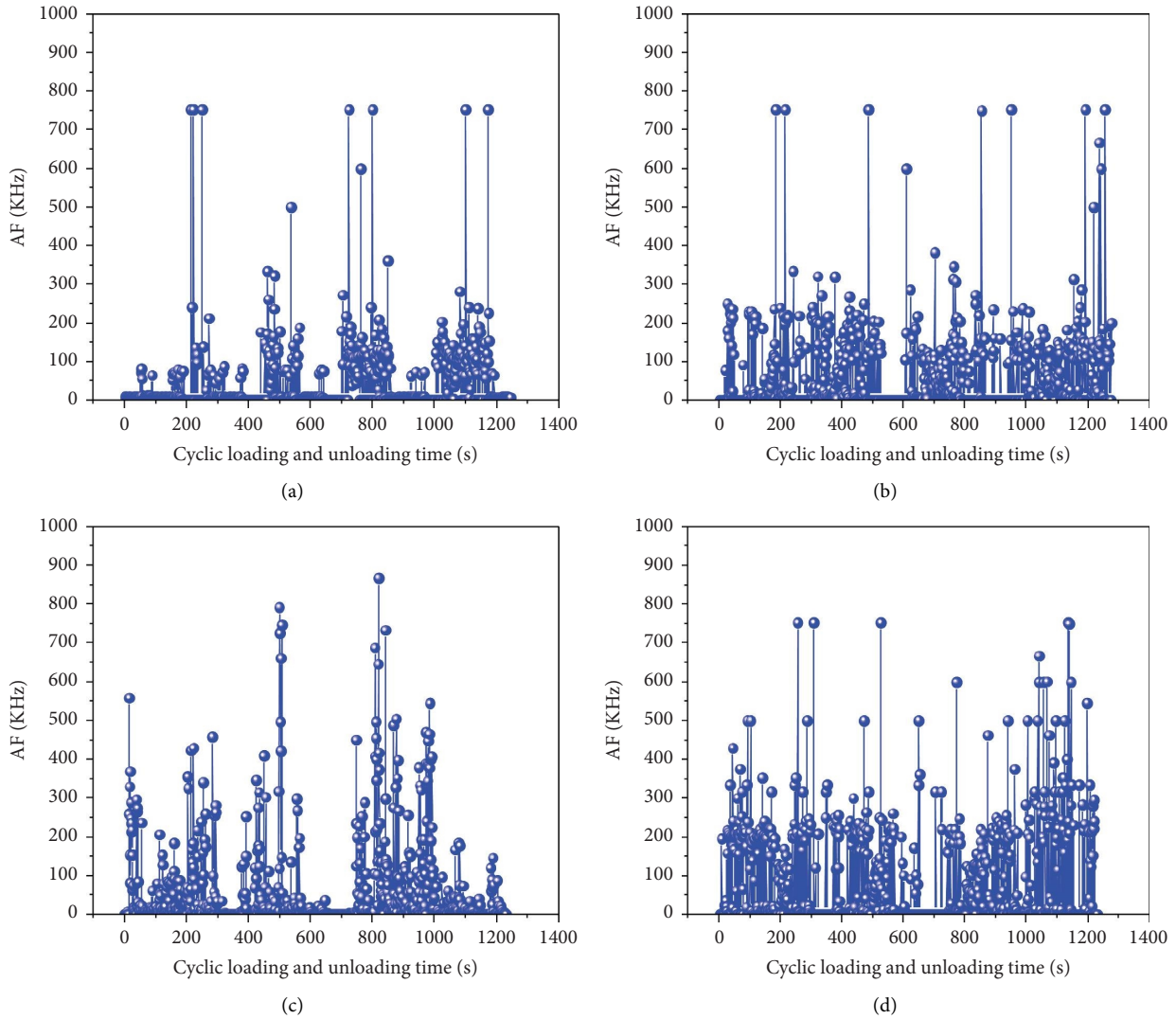

Figure 13: Time history of acoustic-emission AF values of TS-RCR structural bodies with different lithologies. (a) Specimen 1-1#. (b) Specimen 2-1#. (c) Specimen 3-1#. (d) Specimen 4-1#.

lithologies. Figure 12 shows the acoustic-emission damage location of the TS-RCR structural body, and the red dots size represents energy. The blue dots (1-8#) indicate the positions of acoustic-emission sensors.

The TS-RCR structural bodies of different lithologies are subjected to stress under uniaxial cyclic loading and unloading, and stress concentration occurs in local areas. Damage deformations or ruptures occur inside structural bodies, which cause a rapid release of strain energy to produce stress waves. The position of strain-energy releases can be located through the acoustic-emission analyzer. Figures 12(a)–12(d) show the acoustic-emission damage locations of structural bodies 1-1#, 2-1#, 3-1#, and 4-1# with 2,093, 3,961, 5,136, and 6,387 times of positioning, respectively.

The acoustic-emission damage location times of the TS-RCR structural body with different lithologies increase under uniaxial cyclic loading and unloading (Figure 12). TS-RCR structural bodies with different lithologies are more prone to internal damage and deformations under cyclic loading and unloading as the strength of roof and floor rocks becomes weaker. It promotes crack propagation and accelerates the instability and failure of the TS-RCR structural bodies.

The dense location and the high-energy location are mainly distributed in the middle of the TS-RCR structural body. The upper and lower location points of the TS-RCR structural body gradually increase with the weakened strength of the roof and floor rock masses. It is also reflected in another aspect that lithology strength affects the damage

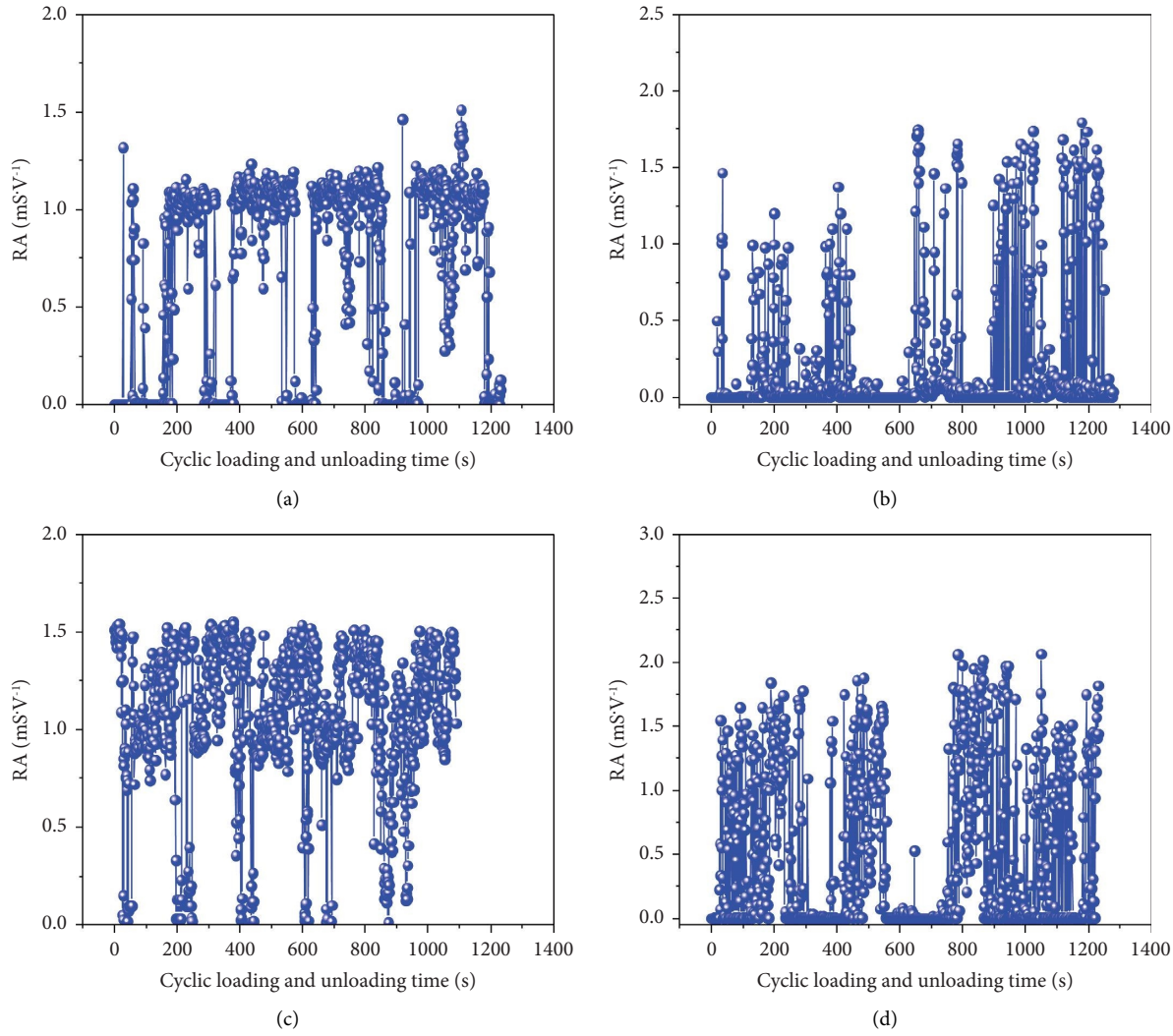

Figure 14: Time history of acoustic-emission RA values of TS-RCR structural bodies with different lithologies. (a) Specimen 1-1#. (b) Specimen 2-1#. (c) Specimen 3-1#. (d) Specimen 4-1#.

deformation and crack propagation of the TS-RCR structural body with different lithologies after cyclic loading and unloading in the uniaxial cycle.

7. Conclusions

(1) The lithofacies assemblages of the roof and floor of the commercial coal seam were listed based on the analysis of the outcrop profile and core data of the 13th commercial coal seam of the Longtan Formation in Xiangshui Coal Mine Area, Guizhou, China. Four representative TS-RCR structural bodies were selected for research, and the mechanical model of the TS-RCR structural body was proposed.

(2) The stress-strain curves of TS-RCR structures with different lithologies under cyclic loading and unloading show a change rule of sparsity, density, and sparsity with the increased cycles. The deformation of TS-RCR structures under cyclic loading and unloading can be divided into four stages. The results of the cyclic loading and unloading test showed that when the height ratio of the TS-RCR structural body was the same, the higher was the strength of the upper and lower rocks, the more was the number of cycles of the TS-RCR structural body, and the denser were the cyclic loading and unloading curves. On the contrary, the lesser the number of cycles of the TS-RCR structural body, the sparser were the cyclic loading and unloading curves.

(3) The results of the nuclear magnetic resonance test showed that the T_2 spectrum curves of the TS-RCR structural bodies were monitored at about 1 and 10 ms, and two obvious peaks were detected. Micropores and mesopores existed in large volumes in the TS-RCR structural body. The signal intensity increased in the relaxation time range of 1 ms, decreased at 10–100 ms, and increased slightly at 100–1,000 ms. The pore structure of the TS-RCR structural body with different lithologies changed significantly with the increased cycle number.

(4) The results of the acoustic-emission test showed that the damage and failure processes of the TS-RCR structural body was roughly divided into three periods according to the time-history analysis of the acoustic-emission AF value of the TS-RCR structural body: the active period with the relatively low AF value ($AF < 60$ kHz) in the 1st and 2nd cycles, the rising period with the relatively stable increased AF value in the 3rd and 4th cycles, and the explosive period with the relatively high AF value ($AF \geq 60$ kHz) in the 5th cycles. According to the relationship between the RA value and time, the evolution law of the RA value and AF value of structures with different lithologies in different periods under cyclic loading and unloading is similar.

Data Availability

The data used to support the findings of this study are included within the article.

Conflicts of Interest

The authors declare that there are no conflicts of interest.

Acknowledgments

This work was supported by the Liupanshui Science and Technology Bureau Fund (52020-2022-PT-15), the Education Department of Guizhou Province Fund (Qianjiaohe KY Zi [2020] 061, Qianjiaohe KY Zi [2020] 050, Qianjiaohe KY Zi [2020] 122, Qianjiao XKTJ [2020] 23, Qianjiaohexietongchuangxinzi [2016] 02, Qianjiaohe KY Zi [2022] 055), the Science and Technology Department of Guizhou Province Fund (QKHJC-ZK[2023]-YB445 and Qiankehe Platform Talent-YSZ [2021] 001), and the Liupanshui Normal University fund (LPSSYYBZK202202).

References

[1] S. Zhang, J. Li, and J. H. Ma, "Roadway supporting technology applied to three soft coal seam at Yanlong mining area in China," *Thermal Science*, vol. 23, no. 3, pp. 887–895, 2019.

[2] C. L. Zhang, D. Y. Ye, P. Yang, S. C. Wu, and C. Wang, "Study on impact tendency of coal and rock mass based on different stress paths," *Advances in Civil Engineering*, vol. 2020, Article ID 8883537, 11 pages, 2020.

[3] S. M. Liu and X. L. Li, "Experimental study on the effect of cold soaking with liquid nitrogen on the coal chemical and microstructural characteristics," *Environmental Science and Pollution Research*, vol. 30, no. 13, pp. 36080–36097, 2022.

[4] S. M. Liu, H. T. Sun, D. M. Zhang et al., "Nuclear magnetic resonance study on the influence of liquid nitrogen cold soaking on the pore structure of different coals," *Physics of Fluids*, vol. 35, no. 1, Article ID 012009, 2023.

[5] S. Yang, G. C. Wen, F. Z. Yan, M. J. Zhang, and X. S. Zhao, "Evaluating the maximum rate of penetration for drilling borehole in soft coal seam," *Energy Science & Engineering*, vol. 8, no. 9, pp. 3273–3284, 2020.

[6] P. S. Cen, E. J. Wei, and K. Y. Tian, "Influence of multistage target temperature and cyclic loading/unloading on the permeability of polypropylene fiber concrete," *Advances in Civil Engineering*, vol. 2022, Article ID 6756069, 11 pages, 2022.

[7] P. Wei, C. W. Huang, X. L. Li, S. J. Peng, and Y. A. Lu, "Numerical simulation of boreholes for gas extraction and effective range of gas extraction in soft coal seams," *Energy Science & Engineering*, vol. 7, no. 5, pp. 1632–1648, 2019.

[8] T. Li, *Experimental Study on Stability of Coal-Rock Structure under Cyclic Loading and Unloading*, Shandong University of Science and Technology, Qingdao, China, 2017.

[9] I. Ben Ammar, C. Karra, A. El Mahi, R. El Guerjouma, and M. Haddar, "Mechanical behavior and acoustic emission technique for detecting damage in sandwich structures," *Applied Acoustics*, vol. 86, pp. 106–117, 2014.

[10] V. L. Shkuratnik, P. V. Nikolenko, and A. E. Koshelev, "Spectral characteristics of acoustic emission in loaded coal specimens for failure prediction," *Journal of Mining Science*, vol. 53, no. 5, pp. 818–823, 2017.

[11] M. He, N. Li, Y. Chen, and C. Zhu, "Strength and fatigue properties of sandstone under dynamic cyclic loading," *Shock and Vibration*, vol. 2016, Article ID 9458582, 8 pages, 2016.

[12] M. N. Bagde and V. Petroš, "Fatigue properties of intact sandstone samples subjected to dynamic uniaxial cyclical loading," *International Journal of Rock Mechanics and Mining Sciences*, vol. 42, no. 2, pp. 237–250, 2005.

[13] Y. B. Cai, K. Wang, and C. Xu, "Comparative experimental study on deformation and damage characteristics of single coal rock and primary coal-rock combination," *Journal of Mining Science and Technology*, vol. 5, no. 3, pp. 278–283, 2020.

[14] W. J. Yu, G. S. Wu, Z. Liu, Y. Lu, Z. Huang, and F. F. Liu, "Experimental study on uneven failure of loose coal and rock compositespecimen," *Coal Science and Technology*, vol. 47, no. 1, pp. 85–90, 2019.

[15] L. M. Dou, C. P. Lu, Z. L. Mu, X. T. Zhang, and Z. H. Li, "Rock burst tendency of coal-rock combinations sample," *Journal of Mining& Safety Engineering*, vol. 23, no. 1, pp. 43–46, 2006.

[16] L. M. Dou, J. C. Tian, C. P. Lu et al., "Research on electromagnetic radlation rules of composed coal-rock burst failure," *Chinese Journal of Rock Mechanics and Engineering*, vol. 24, no. 19, pp. 3341–3344, 2005.

[17] J. P. Zou, Y. Chen, and F. Cui, "Investigation on mechaical properties and rock burst tendency of different coal-rock combined bodies," *Journal of China University of Mining & Technology*, vol. 47, no. 1, pp. 81–87, 2018.

[18] J. P. Zou, J. L. Pei, J. F. Liu, R. D. Peng, and Y. C. Li, "Investigation on acoustic emission behavior and its time-space evolution mechanism in failure process of coal-rock combined body," *Chinese Journal of Rock Mechanics and Engineering*, vol. 30, no. 8, pp. 1564–1570, 2011.

[19] S. J. Chen, D. W. Yin, B. L. Zhang, H. F. Ma, and X. Q. Liu, "Mechanical characteristics and progressive failure mechanism of roof-coal pillar structure," *Chinese Journal of Rock Mechanics and Engineering*, vol. 36, no. 7, pp. 1588–1598, 2017.

[20] X. N. Wang, C. P. Lu, J. H. Xue et al., "Experimental research on rules of acoustic emission and microseismic effects of burst failure of compound coal-rock samples," *Rock and Soil Mechanics*, vol. 34, no. 9, pp. 2569–2575, 2013.

[21] H. G. Li, H. M. Li, and B. B. Gao, "Study on acoustic emission characteristics in the process of fracture of coal-rock combination bodywith different thickness of coal," *Journal of Henan Polytechnic University (Natural Science)*, vol. 40, no. 9, pp. 30–37, 2021.

[22] S. H. Ran, *Experimental Research on Mechanical Properties and Acoustic Emission Characteristics of Red sandstone after Impact Damage*, Jiangxi University of Technology, Ganzhou, China, 2021.

[23] W. Hua, *Study on Mechanical Properties and Damage Evolution Mechanism of Weakly Cemented sandstone under Uniaxial Cyclic Loading and Unloading*, Anhui University of Architecture, Hefei, China, 2021.

[24] Y. J. Zhang, J. T. Li, G. Ma, and S. F. Liu, "Unloading mechanics and energy characteristics of sandstone under different intermediate principal stress conditions," *Advances in Civil Engineering*, vol. 2021, Article ID 5577321, 9 pages, 2021.

[25] W. Huang, J. J. Li, Y. M. Lu et al., "Mechanical properties of soft soil considering the influence of unloading stress paths," *Advances in Civil Engineering*, vol. 2021, Article ID 8813882, 9 pages, 2021.

[26] C. Peng, J. B. Wang, H. X. Liu, G. L. Li, and W. Zhao, "Investigating the macro-micromechanical properties and failure law of granite under loading and unloading conditions," *Advances in Civil Engineering*, vol. 2021, Article ID 9983427, 13 pages, 2021.

[27] J. P. Zuo and H. Q. Song, "Research progress on failure behavior and nonlinear model of deep coal-rock combined bodies," *Journal of Central South University*, vol. 52, no. 8, pp. 2510–2521, 2021.

[28] H. R. Li, Y. F. Qiao, R. X. Shen et al., "Effect of water on mechanical behavior and acoustic emission response of sandstone during loading process: phenomenon and mechanism," *Engineering Geology*, vol. 294, Article ID 106386, 2021.

[29] H. R. Li, Y. F. Qiao, R. X. Shen, and M. C. He, "Electromagnetic radiation signal monitoring and multi-fractal analysis during uniaxial compression of water-bearing sandstone," *Measurement*, vol. 196, Article ID 111245, 2022.

[30] H. R. Li, Y. F. Qiao, M. C. He et al., "Effect of water saturation on dynamic behavior of sandstone after wetting-drying cycles," *Engineering Geology*, vol. 319, Article ID 107105, 2023.

[31] X. P. Xie, H. Y. Liu, X. Q. Fang et al., "Deformation mechanism and control technology of surrounding rock of three-soft coal roadways under high horizontal stress," *Energies*, vol. 16, no. 2, p. 728, 2023.

[32] J. C. Zhang, X. L. Li, Q. Z. Qin, Y. B. Wang, and X. Gao, "Study on overlying strata movement patterns and mechanisms in super-large mining height stopes," *Bulletin of Engineering Geology and the Environment*, vol. 82, no. 4, p. 142, 2023.

[33] H. Y. Liu, B. Y. Zhang, X. L. Li et al., "Research on roof damage mechanism and control technology of gob-side entry retaining under close distance gob," *Engineering Failure Analysis*, vol. 138, no. 5, Article ID 106331, 2022.

[34] H. Y. Liu, B. Y. Zhang, X. L. Li et al., "Influence of geological structures on the occurrence of coalbed methane in Sima coal mine, China," *Frontiers of Earth Science*, vol. 2022, no. 10, Article ID 1000520, 2022.

[35] M. M. He, Y. S. Chen, N. Li, and C. H. Zhu, "Deformation characteristics and energy characteristics of sandstone under uniaxial cyclic loading," *Coal Journal*, vol. 40, no. 8, pp. 1805–1812, 2015.

[36] L. B. Zhang, W. L. Shen, X. L. Li et al., "Abutment pressure distribution law and support analysis of super large mining height face," *International Journal of Environmental Research and Public Health*, vol. 20, no. 1, p. 227, 2022.

[37] X. Y. Zhang, W. L. Shen, Q. Zeng, P. Chen, Q. Qin, and Z. Li, "Research on the mechanism and control technology of coal wall sloughing in the ultra-large mining height working face," *International Journal of Environmental Research and Public Health*, vol. 20, no. 1, p. 868, 2023.

[38] X. P. Lai, S. Zhang, F. Cui, Z. Y. Wang, H. C. Xu, and X. W. Fang, "Energy release law of damage evolution process of water-bearing coal rock and key disaster-pregnant acoustic emission signal picking," *According to Journal of Rock Mechanics and Engineering*, vol. 39, no. 3, pp. 433–444, 2020.

[39] D. G. Yang, Y. X. Zhao, C. Zhang et al., "Experimental study on the effect of cyclic loading on Kaiser effect of sedimentary rock," *Journal of Rock Mechanics and Engineering*, vol. 37, no. 12, pp. 2697–2708, 2018.

[40] G. Han, D. F. Li, L. Q. Chang, X. H. Zhou, and G. Bai, "Experimental research on CH_4 adsorption of different coal samples based on NMR technology," *Journal of Safety Science and Technology*, vol. 17, no. 1, pp. 143–148, 2021.

[41] D. Yue, X. Q. Huo, J. X. Ren et al., "Macro and mesoscopic experimental research on triaxial compression characteristics of fractured coal rock," *Journal of Mining Research and Development*, vol. 42, no. 2, pp. 101–107, 2022.

[42] S. C. Wu, Y. X. Gan, Y. Ren, and L. F. Zhen, "Feasibility of acoustic emission indices based on RA and AF values in tunnel monitoring," *Journal of Engineering Science*, vol. 42, no. 6, pp. 723–730, 2020.

[43] X. L. Li, S. J. Chen, S. M. Liu, and Z. H. Li, "AE waveform characteristics of rock mass under uniaxial loading based on Hilbert-Huang transform," *Journal of Central South University*, vol. 28, no. 6, pp. 1843–1856, 2021.

[44] F. Ren, C. Zhu, and M. He, "Moment tensor analysis of acoustic emissions for cracking mechanisms during schist strain burst," *Rock Mechanics and Rock Engineering*, vol. 53, no. 1, pp. 153–170, 2020.

[45] W. Liu, J. Xu, Z. Wang, and C. Peng, "Experimental research on damage characteristics and safety damage threshold of jointed caverns based on acoustic emissions," *Geomechanics and Geophysics for Geo-Energy and Geo-Resources*, vol. 7, no. 3, pp. 72–14, 2021.

[46] Y. Wang, W. H. Tan, D. Q. Liu, Z. Q. Hou, and C. H. Li, "On anisotropic fracture evolution and energy mechanism during marble failure under uniaxial deformation," *Rock Mechanics and Rock Engineering*, vol. 52, no. 10, pp. 3567–3583, 2019.

[47] H. Q. Duan and D. P. Ma, "Acoustic emission simulation on coal specimen subjected to cyclic loading," *Advances in Civil Engineering*, vol. 2020, Article ID 3798292, 17 pages, 2020.

[48] G. Y. Hou, J. P. Liang, H. Y. Jing, J. X. Tan, Y. G. Zhang, and X. Yang, "Experimental study on deformation and acoustic emission characteristics of arch roadway under different unloading rates," *Advances in Civil Engineering*, vol. 2020, Article ID 8818242, 17 pages, 2020.

[49] Y. Y. Peng, H. X. Deng, M. H. Xing, P. F. Guo, and C. Zhu, "Research on coal mechanical properties based on true triaxial loading and unloading experiment," *Advances in Civil Engineering*, vol. 2021, Article ID 6675222, 10 pages, 2021.

[50] R. X. Shen, H. R. Li, E. Y. Wang et al., "Mechanical behavior and AE and EMR characteristics of natural and saturated coal samples in the indirect tensile process," *Journal of Geophysics and Engineering*, vol. 16, no. 4, pp. 753–763, 2019.

[51] Z. Chong, Q. Yao, X. Li, and K. Shivakumar, "Acoustic emission investigation on scale effect and anisotropy of jointed rock mass by the discrete element method," *Arabian Journal of Geosciences*, vol. 13, no. 9, pp. 324–414, 2020.

[52] Z. Zhang, X. Liu, Y. Zhang, X. Qin, and M. Khan, "Comparative study on fracture characteristics of coal and rock samples based on acoustic emission technology," *Theoretical*

and Applied Fracture Mechanics, vol. 111, Article ID 102851, 2021.

[53] M. Chen, S. Q. Yang, P. G. Ranjith, and Y. C. Zhang, "Cracking behavior of rock containing non-persistent joints with various joints inclinations," *Theoretical and Applied Fracture Mechanics*, vol. 109, Article ID 102701, 2020.

[54] M. Bahaaddini, A. M. Sheikhpourkhani, and H. Mansouri, "Flat-joint model to reproduce the mechanical behaviour of intact rocks," *European Journal of Environmental and Civil Engineering*, vol. 25, no. 8, pp. 1427–1448, 2021.

[55] C. Huang, W. Yang, K. Duan, L. Fang, L. Wang, and C. Bo, "Mechanical behaviors of the brittle rock-like specimens with multi-non-persistent joints under uniaxial compression," *Construction and Building Materials*, vol. 220, pp. 426–443, 2019.

[56] W. Hua, *Study on Mechanical Properties and Damage Evolution Mechanism of Weakly Cemented sandstone under Uniaxial Cyclic Loading and Unloading*, Anhui Jianzhu University, Anhui, China, 2021.

[57] S. H. Ran, *Experimental Study on Mechanical Properties and Acoustic Emission Characteristics of Red sandstone after Impact Damage*, Jiangxi University of Science and Technology, Jiangxi, China, 2021.

[58] S. J. Chen, D. W. Yin, N. Jiang, F. Wang, and W. J. Guo, "Simulation study on effects of loading rate on uniaxial compression failure of composite rock-coal layer," *Geomechanics and Engineering*, vol. 17, no. 4, pp. 333–342, 2019.